Superior Photoelectrocatalytic Performance of Ternary Structural BiVO$_4$/GQD/g-C$_3$N$_4$ Heterojunction

Mohamad Fakhrul Ridhwan Samsudin[a], Habib Ullah[b], Asif A. Tahir[b], Xiaohong Li[b], Yun Hau Ng[c], Suriati Sufian[a, d*]

[a] Chemical Engineering Department, Universiti Teknologi PETRONAS, 32610, Bandar Seri Iskandar, Perak, Malaysia.

[b] Renewable Energy Group, College of Engineering, Mathematics and Physical Sciences, University of Exeter, Penryn Campus, Cornwall, TR10 9FE, United Kingdom

[c] School of Energy and Environment, City University of Hong Kong, Kowloon, Hong Kong SAR, P. R. China.

[d] Centre of Innovative Nanostructures & Nanodevices (COINN), Universiti Teknologi PETRONAS, 32610, Bandar Seri Iskandar, Perak, Malaysia

*Corresponding authors: S. Sufian (suriati@utp.edu.my) Tel: +6053687587

Abstract

Herein, we performed an encyclopedic analysis on the photoelectrocatalytic hydrogen production of $BiVO_4$/g-C_3N_4 decorated with reduced graphene oxide (RGO) or graphene quantum dots (GQDs). The differences between RGO and GQDs as an electron mediator was revealed for the first time in the perspective of theoretical DFT analysis and experimental validation. It was found that the incorporation of GQDs as an electron mediator promotes better photoelectrocatalytic hydrogen performance in comparison to the RGO. The addition of GQD can significantly improve the activity by 25.2 and 75.7% in comparison to the $BiVO_4$/RGO/g-C_3N_4 and binary composite samples, respectively. Correspondingly, the $BiVO_4$/GQD/g-C_3N_4 attained the highest photocurrent density of 19.2 mA/cm^2 with an ABPE of 0.57 % without the presence of any sacrificial reagents. This enhancement is stemming from the low photocharge carrier transfer resistance which was further verified via DFT study. The DFT analysis revealed that the $BiVO_4$/GQD/g-C_3N_4 sample shared their electronic cloud density through orbital hybridization while the $BiVO_4$/RGO/g-C_3N_4 sample show less mutual sharing. Additionally, the charge redistribution of the GQDs-composite at the heterostructure interface articulates a more stable and stronger heterojunction than the RGO-composite. Notably, this study provides new insights on the effect of different carbonaceous materials (RGO and GQDs) which are often used as an electron mediator to enhance photocatalytic activity.

1   Introduction

The burgeoning demand for rapid industrialization had exerted momentous pressure on the global environment. The onslaught of environmental pollution stemming from the overreliance of fossil fuels has provoked environmental threats that could affect the human being[1,2]. Thus, it is imperative to design a new energy technology via the utilization of renewable and sustainable resources in order to minimize the aforementioned environmental threats before it becomes irrevocable issues. Drawing inspiration from natural photosynthesis, photocatalytic water splitting via photocatalyst materials for the production of sustainable hydrogen energy has been regarded as a judicious strategy for future energy generation [3].

Bismuth vanadate ($BiVO_4$) has galvanized heightened interest among the scientific community as a promising material with peculiar photocatalytic features including moderate bandgap energy, excellent photochemical stability and environmentally friendly materials [4,5]. Generally, $BiVO_4$ exists in three different crystal structures which are monoclinic clinobisvanite, orthorhombic pucherite and tetragonal dreyerite in which all of these structures possess different photocatalytic activity upon light illumination [6]. For example, the monoclinic structure was composed of additional Bi 6s orbitals in the valance band which allows a short transition of photocharge carriers to the V 3d orbitals in the conduction band and thus corresponds to the smaller bandgap energy. Meanwhile, the tetragonal structure was made up of only O 2p orbitals, consequently, lengthen the transition of the photocharge carrier which can promote the recombination rate and limits the photocatalytic performance. Nevertheless, there are several bottleneck issues of the pure $BiVO_4$ which has hindered the overall practicality of this semiconductor material [7,8].

63   Hitherto, various efforts have been performed in mitigating the inherent limitations of $BiVO_4$

64   such as the formation of the heterostructure systems, introducing defects structures and

65   nanoscaling [9]. Amidst the proposed strategies, the heterostructure system approach has been

66   regarded as a promising strategy to significantly boost the photocatalytic performance owing to its

67   smooth photocharge separation and migration; and limited photocharge recombination. [10,11].

68   Recently, graphitic carbon nitride ($g-C_3N_4$) photocatalyst has drawn prime attention in the area of

69   photocatalyst as a metal-free polymeric two-dimensional (2D) materials with medium bandgap

70   energy [12,13]. The structural advantages of the $g-C_3N_4$ such as high thermal stability, direct

71   bandgap and appropriate flat band potential for hydrogen evolution suggest a complementary

72   heterostructure combination with the $BiVO_4$ [11,14]. For example, Wang et al. [15] developed g-

73    $C_3N_4/BiVO_4$ photocatalyst with a high photocurrent density of 0.44 mA/cm^2 at 0.56 V in the linear

74   sweep current-voltage test. Subsequently, Safaei et al. [16] revealed that the $g-C_3N_4/BiVO_4$

75   achieved high photocurrent density of 0.42 mA/cm^2 at 1.23 V vs. RHE which was attributed to the

76   lower charge transfer resistance and high oxygen vacancy sites. However, the $g-C_3N_4/BiVO_4$

77   sample often possesses the Type II heterostructure system which has limited photocharge carrier

78   redox abilities and not favourable for solar hydrogen production as it requires high redox potential

79   of H_2/H^+. Recently, we have reported the promising potential of RGO as an electron mediator for

80   mitigating the limitation that exists within the Type II system [17]. The addition of RGO has

81   modified the Type II system into the novel Z-scheme system which possesses strong oxidation and

82   reduction capability between the sample and fulfils the prerequisite of the solar hydrogen

83   production [18,19].

84   Notwithstanding the promising potential of the aforementioned binary system, the discussion

85   on the effect of the different geometrical structures of the graphene-based materials, particularly

86　RGO and GQDs on enhancing the heterostructure photocatalytic performances are often not been

87　exhaustively scrutinized. Additionally, to the extent of authors' knowledge, the study on

88　photoelectrocatalytic hydrogen evolution using natural lake water without sacrificial reagents

89　instead of the chemical-based electrolyte solution is limited.

90　　　Due to these Achilles' heels, our group aims to provide an insight into all of these

91　unanswerable questions by developing the $BiVO_4/g-C_3N_4$ heterostructure photocatalyst with the

92　addition of RGO or GQD for the first time. We evaluate the ternary structural differences via

93　photoelectrocatalytic hydrogen production using natural lake water. The differences between both

94　RGO and GQD as electron mediators were revealed in the view of experimental and DFT analysis.

95　We systematically analyse the structural properties of each of the studied photocatalyst either in

96　the pure form, binary structure and ternary heterostructure system. The electronic properties of

97　these models are simulated to countercheck our experimental data. Simulated electronic properties

98　include band structure (valence band, conduction band, and bandgap), the partial density of states

99　(PDOS), Fermi energy level, electrostatic potential, charge difference density (CDD), surface

100　formation energy and adsorption energy of water molecule.

101

2　Materials and Methods

2.1　Preparation of Photocatalyst Sample

104　　　The details of the purity and assay of the raw materials used in the synthesizing of the

105　photocatalysts have been included in Supplementary Information. Generally, the pure $BiVO_4$ and

106　$g-C_3N_4$ were individually prepared via a modified hydrothermal method and thermal

107　polycondensation of urea, respectively. The details of these synthesizing protocols can be found

108 elsewhere [7]. Meanwhile, the RGO was synthesized using a modified Hummer's method reported

109 by Samsudin et al. [17] and GQDs were prepared according to the previously reported literature

110 [20]. For the binary $BiVO_4$/g-C_3N_4 sample, a wet-impregnation technique was applied to prepare

111 this composite in which 0.8 wt.% of g-C_3N_4 was thoroughly mixed with 1 g of $BiVO_4$ in 40 mL of

112 deionized water. Details of the procedure have been reported previously [7]. The same synthesis

113 protocols were applied in preparing the ternary $BiVO_4$/RGO/g-C_3N_4 and $BiVO_4$/GQD/g-C_3N_4

114 samples in which each of the ternary structure contains 0.8 wt.% of the graphene-based materials.

2.2 PEC Measurement

116 The physicochemical properties of the photocatalysts were thoroughly examined via X-ray

117 diffraction (XRD), Brunauer-Emmet-Teller (BET), X-ray Photoelectron Spectroscopy (XPS),

118 Fourier Transform Infrared (FTIR) spectra, Field-Emission Scanning Electron Microscopy

119 (FESEM) and High-Resolution Transmission Electron Microscopy (HRTEM) in which details of

120 these measurements can be found in the Supplementary Information. Meanwhile, the PEC analysis

121 was performed in a standard three-cell configuration system using an Autolab potentiostat

122 PGSTAT302N (Metrohm). The fabrication method for preparing the photoanode (working

123 electrode) containing as-developed photocatalyst was detailed in our previous publication [21].

124 Meanwhile, the reference and counter electrodes were made up of Ag/AgCl and Platinum rod.

125 Additionally, 0.5 M Na_2SO_4 and 500 W halogen lamp (AM 1.5G illumination) were employed as

126 an electrolyte and visible-light-source. Furthermore, the I-V curves were measured using a Linear

127 Sweep Voltammetry (LSV) procedure while the EIS was analyzed using a frequency response

128 analyzer (FRA). Specific details on the measurement have been described previously [7].

2.3 Photoelectrocatalytic Hydrogen Evolution

The photoelectrocatalytic hydrogen production was measured in a PEC-DSSCs setup as illustrated in Figure S1. The working anode was made up of the as-developed photoanode and the counter electrode was made up of platinum rod which was connected with DSSCs in a series arrangement to provide external bias energy. A 200 mL of natural lake water with pH 7.2 was used as a water source. The produced hydrogen analysed using Multiple Gas Analyzer software (SRI Instruments 8610-0071) equipped with TCD and a molecular sieve 13 X columns.

2.4 Density Functional Theory Calculations

DFT calculations were performed on QuantumATK and the results were visualized on VESTA and Virtual NanoLab Version 2019.12. The details on the lattice parameters, hall symmetry, slab model calculations for surface energies and band edge locations, and other related DFT protocols for the pure $BiVO_4$ and g-C_3N_4 has been well described in our recent paper [7]. Similarly, the protocols for measuring the surface formation energy and electrostatic potentials were included in our previous reports [16,22,23]. Meanwhile, in the case of RGO, GQDs, and g-C_3N_4, we used a single layer structure for the aforementioned analysis. Furthermore, in order to represent and counterchecked the experimental data, we built the following models of photocatalyst which include the $BiVO_4$/GQDs, $BiVO_4$/RGO, $BiVO_4$/g-C_3N_4, $BiVO_4$/GQDs/g-C_3N_4, and $BiVO_4$/RGO/g-C_3N_4 heterostructures. The single layer of RGO, GQD, and g-C_3N_4 were adsorbed on the optimized surface of $BiVO_4$ (*vide infra*). In order to avoid a higher mismatch in the heterojunctions, the cell parameters of all these species were kept similar. Geometries of all these species were optimized at generalized gradient approximation (GGA) with the Perdew-Burke-Ernzerhof (PBE) exchange-correlation functional and double Zeta Polarized (DZP) basis

7

151 set [24]. Linear combination of atomic orbitals (LCAO) method has been employed for Bi, V, C,

152 N, H, and O atoms [25]. Different types and sizes of the Monkhorst-Pack k-grid and energy cutoff

153 were employed for each individual sample. The TB09LDA functional of meta-GGA was

154 performed to estimate the band structure properties by embedding with the Tran and Blaha XC

155 functional equation [25]. Furthermore, we also measured the DOS, PDOS, band structure, EDD,

156 electrostatic potential, and effective masses of the charge carriers according to the protocols

157 described by Endres et al. [26].

3   Results and Discussion

3.1   FTIR Analysis

160   Figure 1(a) manifests the Fourier Transform Infrared (FTIR) spectra of all of the as-

161 developed photocatalyst. The FTIR spectra of the pure $BiVO_4$ and $g-C_3N_4$ sample has been

162 comprehensively discussed in our previous publication [21,27]. Generally, the pure $BiVO_4$ was

163 made up of a broad peak and weak shoulder located around 750 cm^{-1} ($v3$ of the VO_4^{3-}) and 530

164 cm^{-1} ($v4$ of the VO_4^{3-}) [17]. Moreover, the observed broad and small FTIR peaks monitored at

165 3460 and 1500 cm^{-1}, respectively were stemming from the O−H stretching and O−H bending

166 mode, respectively [28]. The presence of the $g-C_3N_4$ photocatalyst was verified through the

167 detection of the triazine units which can be detected at 813 cm^{-1} [29].

168   Furthermore, the multiple peaks in the range 1300 – 1500 cm^{-1} corresponds to the typical

169 stretching modes of C−N heterocycles [30]. The small peak located at 1240 and 1317 cm^{-1} were

170 attributed to the partial condensation of C−NH−C and full condensation of C−N(−C) −C units,

171 respectively. It is conspicuous that the heterostructure samples exemplified identical characteristic

172 peaks of parent $BiVO_4$ and $g-C_3N_4$, highlighting that the $BiVO_4/g-C_3N_4$ heterostructure was

8

synthesized successfully. Interestingly, the FTIR patterns for the binary and ternary structure samples were almost identical with no evident signal of RGO and GQDs were detected. These similar FTIR patterns among the binary and ternary samples can be occurred due to the low loading amount of graphene-based materials used in this study.
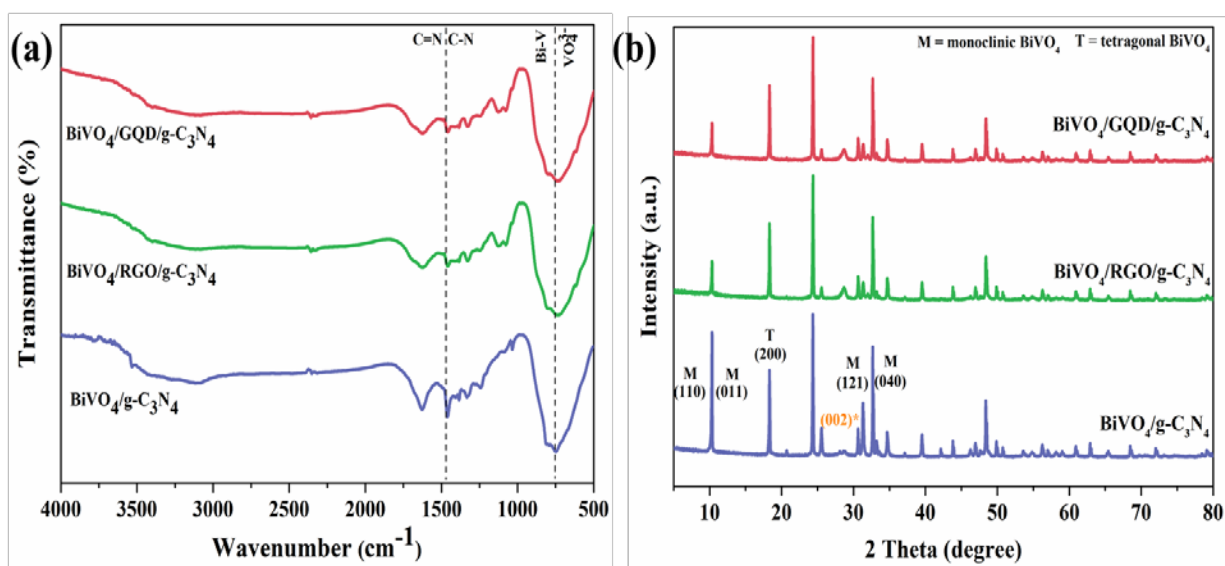
Figure 1: (a) FTIR spectra and (b) XRD spectra of the as-developed photocatalyst.

3.2 XRD, FESEM and TEM Properties

The XRD analysis revealed that the photocatalyst sample feature two different crystallographic properties which were tetragonal and monoclinic structure, corresponds to the $BiVO_4$ properties as shown in Figure 1 (b). The peaks of the monoclinic structure located at 10.2, 10.9, 30.6, 31.5 and 32.6° of 2θ while the peaks of the tetragonal structure located at 24.6 and 25.3° of 2θ. Both crystal structures can be indexed to the JCPDS card no. 14−0688 and JCPDS card no. 14−0133 [21]. Meanwhile, peak detected at 28.5° of 2θ was belongs to the (002) facet of the g-C_3N_4 [31]. Nevertheless, there are no XRD diffraction peaks appeared corresponded to the

9

187 RGO and GQDs, presumably due to the low content and high dispersity in the heterostructure

188 sample.
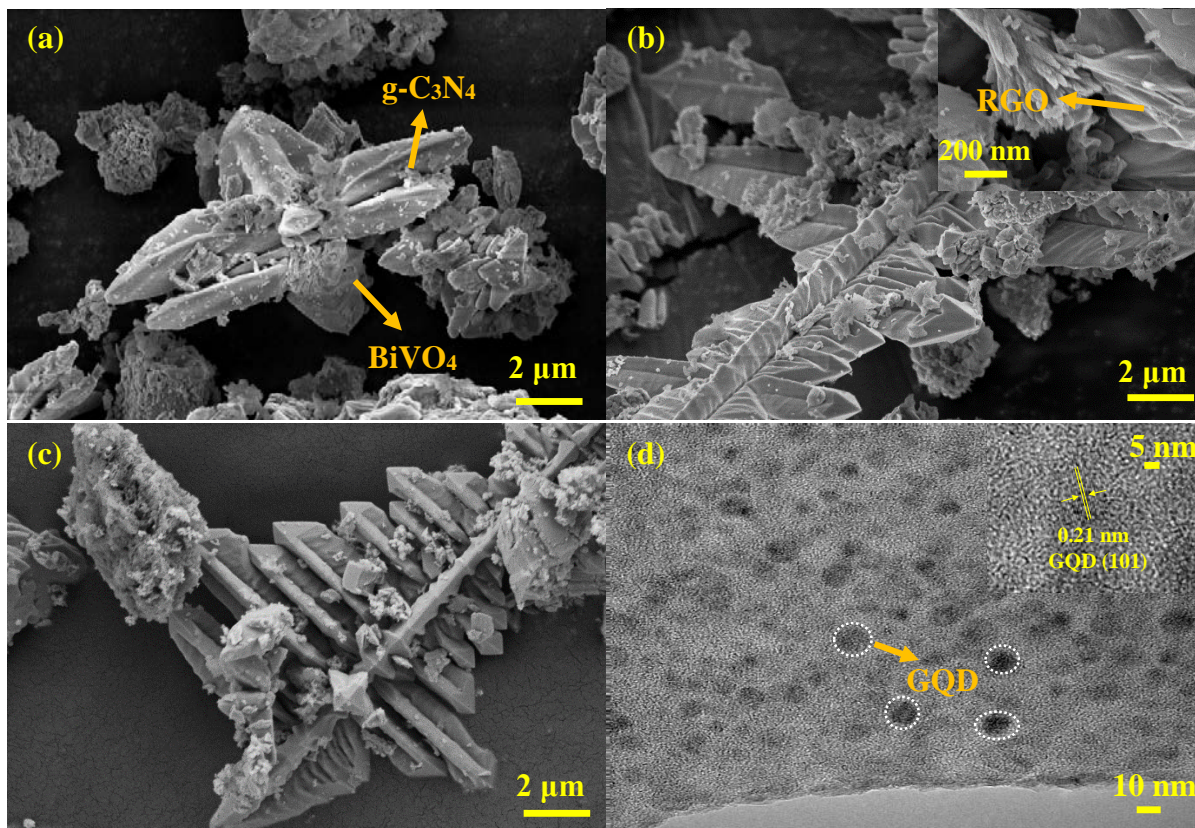
190 Figure 2: FESEM micrograph images of (a) $BiVO_4$/g-C_3N_4, (b) $BiVO_4$/RGO/g-C_3N_4 (inset is the

191 200 nm zoom micrograph image which detect the RGO layer in the composite sample), (c)

192 $BiVO_4$/GQD/g-C_3N_4 and (d) HRTEM image of GQD.

194 The morphological structures of the binary and ternary heterostructure photocatalysts were

195 scrutinized using FESEM and TEM. As depicted in Figure 2, the FESEM images revealed that the

196 $BiVO_4$ possesses the typical microflower shape like structure with distinctly sharp edges. Notably,

197 the crumple two-dimensional (2D) porous structure was randomly distributed on the surface of the

198 $BiVO_4$ microflower corresponded to the g-C_3N_4, manifesting the intimate contact between $BiVO_4$

199   and g-C$_3$N$_4$ particles. The inset FESEM image in Figure 2 (b) indicates the presence of the

200   wrinkled thin-silk structure of RGO originated from the decomposition of the oxygen functional

201   groups that leads to graphene-like sheets with a disordered stacking [32]. The detection of RGO

202   in the heterostructure BiVO$_4$/RGO/g-C$_3$N$_4$ sample signifies the successful fabrication of the

203   composite sample.

204   Similarly, the BiVO$_4$/GQD/g-C$_3$N$_4$ sample exemplifies the typical identical morphological

205   structure of individual BiVO$_4$ and g-C$_3$N$_4$. However, there is no morphological structure

206   corresponded to GQD was detected in the FESEM micrograph image, presumably due to the small

207   size. Figure 2 (d) exhibits the HRTEM image of the as-developed GQDs which have a diameter

208   range of 5 – 9 nm. The lattices of GQD can be clearly observed, attaining a high crystallization

209   level of GQDs. The interplanar spacing of GQDs is 0.21 nm which coincides well with typical

210   (101) spacing of graphitic carbon [33,34]. Furthermore, the top and cross-sectional FESEM images

211   along with the EDX and elemental mapping of the BiVO$_4$/RGO/g-C$_3$N$_4$ and BiVO$_4$/GQD/g-C$_3$N$_4$

212   were demonstrated in Figure S2 and S3 which clearly suggesting the presence of all elemental

213   footprints corresponds to the parental BiVO$_4$, RGO, GQD and g-C$_3$N$_4$ sample.

214   **3.4   Optical Properties**

215   Previously, we report that the pure BiVO$_4$ and g-C$_3$N$_4$ photocatalyst possesses an absorption

216   edge around 520 and 430 nm, conforming to bandgap energy of 2.40 and 2.80 eV, respectively

217   [35–38]. Meanwhile, the binary BiVO$_4$/g-C$_3$N$_4$ exhibits slightly increased in absorption intensity

218   at 530 nm as shown in Figure 3 (a), evincing that the hybridization of individual photocatalyst

219   does improve the light absorption capacity near the visible-light region. Meanwhile, both of the

220   ternary heterostructure samples manifest an almost similar absorption edge in comparison to the

221   binary structure. Based on Figure 3 (b), it was estimated that the bandgap energy of $BiVO_4/g\text{-}C_3N_4$,

222    $BiVO_4/RGO/g\text{-}C_3N_4$ and $BiVO_4/GQD/g\text{-}C_3N_4$ samples were calculated to be 2.74, 2.52 and 2.47

223   eV. It is worth noting that the addition of RGO and GQDs as an electron mediator further enhanced

224   the absorption capacity of the composite materials near the visible-light region, results in

225   significant enhancement on the photoelectrocatalytic performance. Moreover, the RGO and GQDs

226   can act as a photosensitizer for bandgap narrowing, endowing efficient electron-hole pairs

227   separation and hindered the photocharge carrier recombination.
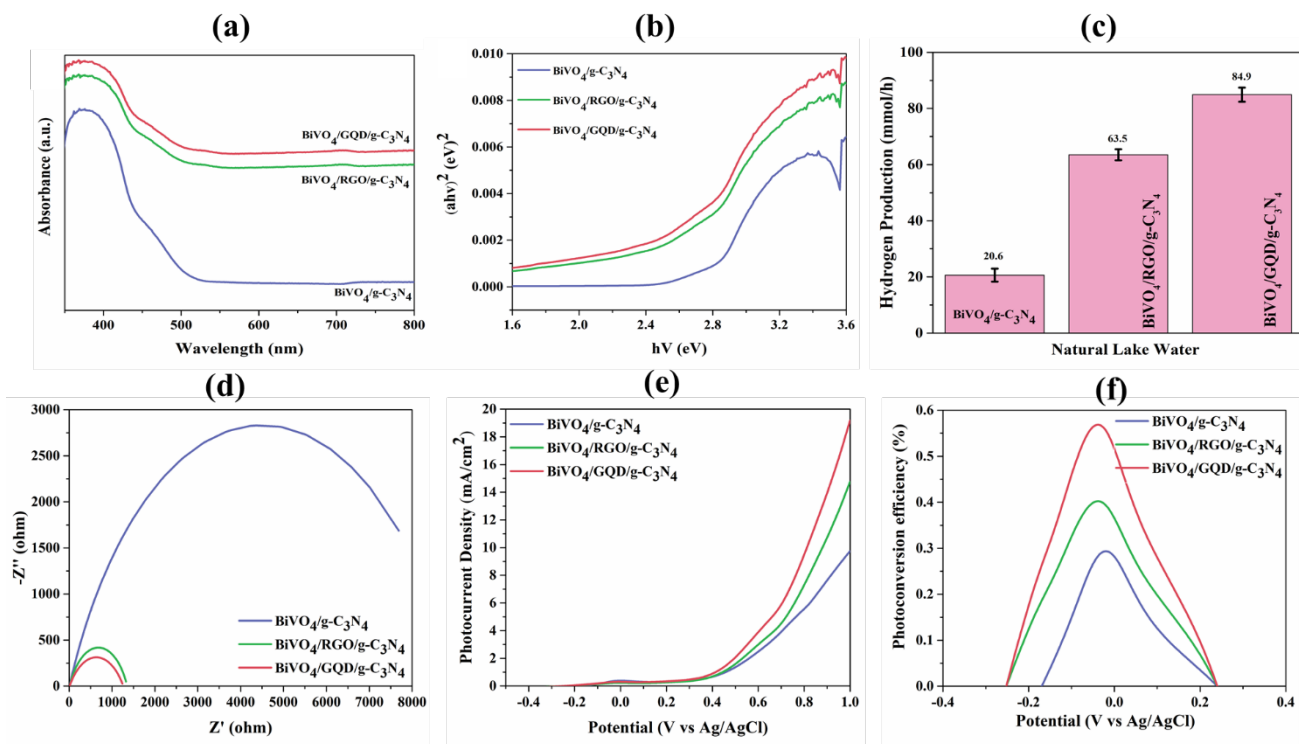
228

229   Figure 3: (a) Absorbance spectra, (b) Tauc plot, (c) Photoelectrocatalytic hydrogen production,
230   (d) EIS Nyquist plot, (e) Photocurrent density, and (f) Photoconversion efficiency of the as-
231   developed photocatalyst.

3.5 BET Analysis

Figure S4 depicts the N_2 adsorption-desorption isotherms of the binary and ternary heterostructure photocatalysts. The linear isotherm plot exemplifies the characteristic nature of Type IV isotherms with the H3-type hysteresis loop at a relatively high P/P_0 of 0.7 – 1.0. Additionally, the details on the BET analysis of the composite photocatalysts were summarized in Table 1. The BET surface area, pore volume and pore size of $BiVO_4/g-C_3N_4$ were 5.20 m^2g^{-1}, 0.023 cm^3g^{-1} and 22.05 nm. Nevertheless, when the RGO and GQDs were incorporated into the ternary heterostructure, the BET surface area was slightly decreased. This phenomenon can be explained due to the potential blockage of some of the active sites by the RGO and GQDs.

Table 1: BET specific surface area, pore volume and pore size of the as-developed photocatalyst.

Sample	S_{BET} (m^2g^{-1})	Pore Volume (cm^3g^{-1})	Pore Size (nm)
$BiVO_4/ g-C_3N_4$	5.20	0.023	22.05
$BiVO_4/RGO/g-C_3N_4$	4.53	0.019	20.40
$BiVO_4/GQD/g-C_3N_4$	4.39	0.018	18.57

3.6 Photoelectrocatalytic Hydrogen Production

The performance of the binary and ternary heterostructure samples was evaluated using natural lake water as illustrated in Figure 3 (c). There is no chemical electrolyte was added during the measurement in order to highlight the potential of green hydrogen production via natural water sources. Previously, our group reported that the photoelectrocatalytic hydrogen performance of the pure $BiVO_4$ and $g-C_3N_4$ were found to be 9.5 and 11.9 mmol/h [21]. The low photoelectrocatalytic performance for pure samples was stemming from its natural limitation which is the fast recombination rate of the photogenerated charge carriers [6,19]. Interestingly, the hybridization of $BiVO_4$ and $g-C_3N_4$ to form the heterostructure system significantly enhanced photoelectrocatalytic

252 activity despite being without any sacrificial reagents. Moreover, the addition of RGO in the

253 ternary heterostructure system has a substantial effect on the performance compared to the binary

254 system. The high photoelectrochemical hydrogen production of 63.5 mmol demonstrated by the

255 $BiVO_4/RGO/g-C_3N_4$ sample implying that the RGO serves as an excellent electron mediator for

256 the reduction process which lowers the photocatalytic overpotential and thus minimizing the

257 photocharge carrier recombination [39]. Moreover, the intimate interfacial interaction between the

258 individual photocatalyst with the RGO, evidently from the FESEM micrograph image does allow

259 a smooth and efficient photocharge carrier separation and migration between the adjacent

260 photocatalyst. This phenomenon is aligned with principle akin to other reported studies, whereby

261 the addition of the RGO does help in boosting the photocatalytic activity [17,40,41].

262 Interestingly, the formation of the ternary heterostructure with the GQDs material

263 demonstrates the highest photoelectrocatalytic activity of 84.9 mmol/h which was ~25% higher

264 than the composite sample with RGO as an electron mediator. This scenario could be attributed to

265 the strong quantum confinement effect and boundary effect of GQDs owing to its smaller size

266 below 10 nm in comparison to the RGO which typically size range below 100 nm [42]. Moreover,

267 the hybridization of GQDs in the composite heterostructure system not only promotes the π-

268 electron delocalization, but also creates a new photocharge carrier separation and migration

269 pathways with lower energy, results in enhancement of visible-light harvesting [43].

270 **3.7 Photoelectrochemical (PEC) Behaviour Analysis**

271 The EIS analysis was used to examine the properties of the photocharge carrier separation

272 and migration within the binary and ternary structure as shown in Figure 3 (d). Generally, the

14

273   semicircle arc radius on the EIS Nyquist plot indicating the photocharge carrier resistance in which

274   the bigger the arc radii, the higher the resistance, consequently jeopardizing the photocatalytic

275   performance. As reported in our work previously [21,27,44], the EIS Nyquist plot for the pure

276    $BiVO_4$ and $g-C_3N_4$ shows a bigger semicircle arc diameter with high photocharge carrier resistance

277   due to its inherent limitation as single photocatalyst materials [45]. However, the observed

278   semicircle arc diameter of the ternary heterostructure possesses a small diameter than the binary

279   heterostructure. This observation signifying the robust interfacial photocharge carrier migration

280   and separation through the ternary heterostructure with the aids of either RGO or GQDs.

281   Comparatively, the $BiVO_4/GQD/g-C_3N_4$ sample exhibit the smallest semicircle arc diameter than

282    $BiVO_4/RGO/g-C_3N_4$ sample, indicating that the GQD serve better as an electron mediator at the

283   interface heterojunction than RGO.

284   The current-potential (I-V) curve of the studied photocatalyst was demonstrated in Figure 3

285   (e). The binary $BiVO_4/g-C_3N_4$ attained a photocurrent density of 9.62 mA/cm^2 which is higher

286   than the pure sample as reported by our group previously [21]. Interestingly, the photocurrent

287   density of the binary $BiVO_4/g-C_3N_4$ sample integrated either with RGO or GQD was considerably

288   higher relative to the sample without an electron mediator, signifying that the ternary

289   heterostructure sample has excellent photocharge carrier separation and migration upon light

290   illumination. In addition, the ternary heterostructure embedded with the RGO achieved a

291   photocurrent density of 14.6 mA/cm^2 while the ternary heterostructure sample integrated with the

292   GQD exhibit the highest photocurrent density of 19.2 mA/cm^2 at 1.0 V vs Ag/AgCl. The enhanced

293   by 24% of the photocurrent density by composite sample integrated with GQD compare to RGO

294   further corroborated the EIS Nyquist analysis that the GQD serves better as an electron mediator

295   at the interface heterojunction with a minimal photocharge carrier resistance.

296   The ABPE was measured to examine the relationship between the applied voltage and

297   photocurrent density and the details on the ABPE can be referred elsewhere [8,38,45]. Previously,

298   our group reported that the ABPE of the pure $BiVO_4$ was only 0.056% in which confirming the

299   limited photocatalytic nature of the single photocatalyst. However, after constructing the binary

300   system with $g-C_3N_4$, the ABPE of this sample reaches 0.29%, indicating an 80% improvement in

301   the ABPE when $BiVO_4$ has formed a heterostructure system with the $g-C_3N_4$. Meanwhile, the

302   formation of the ternary heterostructure sample with the RGO demonstrates superior ABPE with

303   0.40% efficiency at -0.03 V vs. Ag/AgCl. Concomitant with this, the ternary heterostructure

304   sample embedded with the GQDs displays the highest photoconversion efficiency (0.57%) in

305   comparison to other samples as illustrates in Figure 3 (f). Such results can be ascribed to the

306   decrease in the photocharge resistance at the electrode/electrolyte interface induced by the

307   quantum size of GQD, evidently from the EIS Nyquist plot. Furthermore, the hybridization of

308   GQD not only improved the ABPE of the composite $BiVO_4/g-C_3N_4$ sample, but also significantly

309   improved the resistance of the as-developed photocatalyst against photocorrosion, affirming it

310   position as a frontier photocatalyst for a wide range of photocatalytic applications.

311   **3.8 Photoelectrocatalytic Stability and Recyclability**

312   The stability and recyclability analysis of the $BiVO_4/GQD/g-C_3N_4$ was essential for

313   demonstrating its practical applications as the photocorrosion is one of the major limiting factors

314   that affecting the photocatalytic activity. Figure 4 (a) demonstrates the stability and recyclability

315   performance of the ternary heterostructure sample for three cyclic activity. It can be seen that the

316   ternary heterostructure sample manifests an excellent photostability with only a 3.6% loss in

317   comparison to the first cycle. The minimal loss in the hydrogen evolution performance inferred on

16

318 the great BiVO$_4$/GQD/g-C$_3$N$_4$ stability against photocorrosion. Furthermore, we further justified

319 the excellent photostability of this ternary heterostructure by comparing its XRD analysis before

320 and after the performance testing. Figure 4 (b) shows that there is no noticeable change in the

321 crystallographic structure of the BiVO$_4$/GQD/g-C$_3$N$_4$ sample was monitored in comparison to the

322 fresh sample even after three cyclic activity. These results further corroborated that the as-

323 developed BiVO$_4$/GQD/g-C$_3$N$_4$ sample possesses exceptional stability against photocorrosion in

324 which signifying the practicality of this developed material.
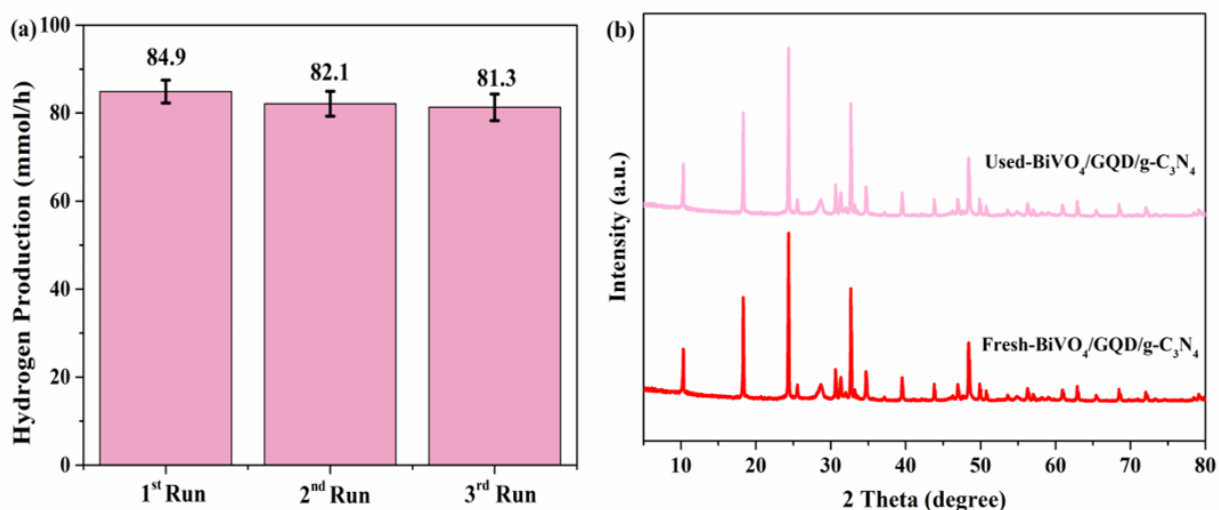
325

326
327 Figure 4: (a) Photoelectrocatalytic stability and recyclability and (b) XRD analysis of the
BiVO$_4$/GQD/g-C$_3$N$_4$ photocatalyst under visible-light-irradiation.

328 ### 3.9 DFT Analysis

329 As discussed in the experimental section, the ternary BiVO$_4$/GQD/g-C$_3$N$_4$ sample was

330 superior to the RGO-ternary heterostructure. So, in order to correlate and confirm our observation;

331 we performed DFT analysis for bare samples including BiVO$_4$, g-C$_3$N$_4$, RGO, GQD, and also for

332 the binary and ternary heterostructure samples which include BiVO$_4$/g-C$_3$N$_4$, BiVO$_4$/GQD,

17

333   BiVO$_4$/RGO, BiVO$_4$/RGO/g-C$_3$N$_4$ and BiVO$_4$/GQD/g-C$_3$N$_4$ heterostructures. The optimized

334   relaxed structures of the investigated models are given in Figure 5. The positive value (1.95 J/m^2)

335   monitored from the surface formation energy of BiVO$_4$ indicates that the sample retains a stable

336   and non-polar characteristic [46]. Thus, the slab of BiVO$_4$ was chosen to construct the mentioned

337   binary and ternary heterostructures, with almost no lattice mismatch (0.02 %).

338
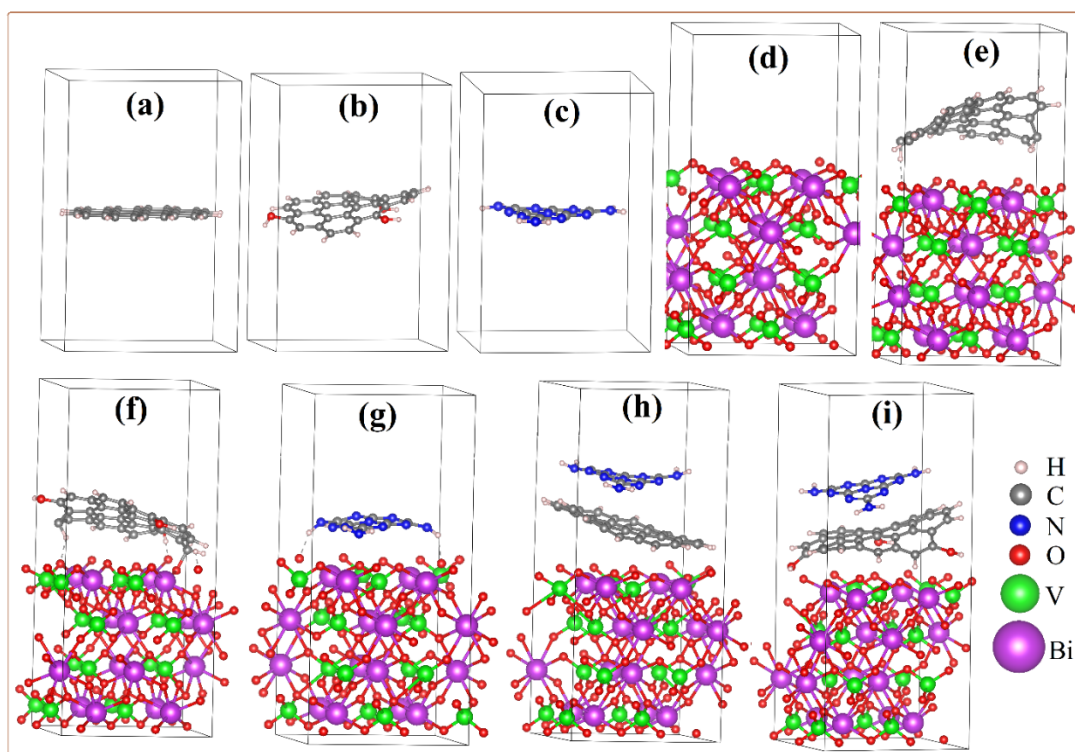
339
340   Figure 5: Optimized geometries of (a) GQDs, (b) RGO, (c) g-C$_3$N$_4$, (d) BiVO$_4$, (e)
       BiVO$_4$/GQDs, (f) BiVO$_4$/RGO, (g) BiVO$_4$/g-C$_3$N$_4$, (h) BiVO$_4$/GQDs/g-C$_3$N$_4$, and (i)
341   BiVO$_4$/RGO/g-C$_3$N$_4$ systems. The lattice mismatch in the heterojunctions are less than 0.02%.

342

343   The successful incorporation of RGO, GQD, and g-C$_3$N$_4$ on the surface of BiVO$_4$ was

344   confirmed from their strong interaction energy, charge transfer, and electrostatic potential map.

345   These can be seen from a strong electrostatic interaction of a non-covalent nature that was

18

346 developed with the Bi—N, Bi—C, O—C, O—N and H—O inter-bonding. Correspondingly, the

347 calculated interaction/adsorption energy of these interactions was in the range of -0.58 to -0.83 eV,

348 indicate the binary and ternary heterostructures were thermodynamically stable. The

349 aforementioned energy value was calculated based on the following equation:

350 $$\Delta E_{ad} = E_{Product} - (E_{Reactant\ 1} + E_{Reactant\ 2}) \tag{1}$$

351 Where $E_{(Product)}$, $E_{Reactant\ 1}$, and $E_{Reactant\ 2}$ are the sum of the energy of the relaxed composite

352 system, layer(s) of RGO, GQD, and g-C$_3$N$_4$, and BiVO$_4$, respectively. Comparative analysis of the

353 electrostatic potential maps of all the investigated species led us to predict that BiVO$_4$/GQD/g-

354 C$_3$N$_4$ was more stable than others. This can be seen from its homogeneous distribution of

355 electrostatic potential maps, especially at the interface as shown in Figure 6.

(a)   **(b)**   **(c)**

356
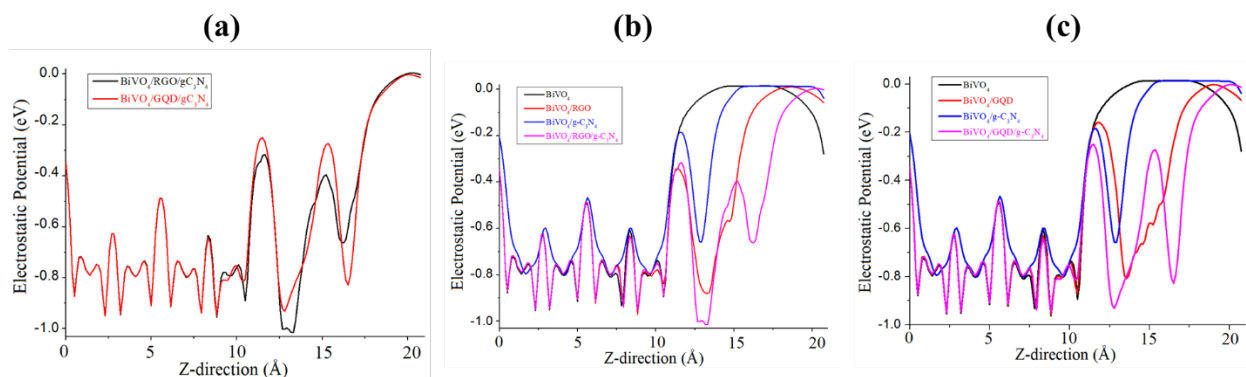
357
358 Figure 6: (a) 1-D projection of the electrostatic potential maps of BiVO$_4$/RGO/g-C$_3$N$_4$ (black
line) and BiVO$_4$/RGO/g-C$_3$N$_4$ (red line) heterojunctions; and 1-D projection of the electrostatic
359 potential maps of (b) BiVO$_4$/RGO/g-C$_3$N$_4$ and (c) BiVO$_4$/GQD/g-C$_3$N$_4$ heterojunctions.

360

361 In addition, the inter-charge transfer within both ternary heterostructure samples was

362 estimated with the help of charge density difference (CDD), and the results were shown in Figure

19

363 7, while that of other species was shown in Figure S5 and S6. Based on Figure 7, there are two

364 areas under the curve was coloured in yellow which corresponds to the accumulation of the charge.

365 Meanwhile, the green coloured curve represents the depletion charge region. It can be seen that

366 the charge distribution of both ternary heterostructure samples dominantly occurs at the interface

367 region. However, there was no accumulation and depletion region were observed on $BiVO_4$;

368 especially those parts which were far away from the interface. This phenomenon is important as it

369 was responsible for creating an electric field at the heterostructure interface, results in enhancing

370 the separation and migration of the photocharge carriers (*vide supra*). Moreover, the observed

371 charge distribution patterns indicate the formation of a weak Vander Waal type interaction between

372 the individual samples [47]. Therefore, it can be concluded that the studied ternary heterostructure

373 system possesses a typical p-n heterojunction system [48].

374   On the other hand, a slice of the planar-averaged CDD for both the ternary heterostructure

375 system, along with the Z-direction was illustrated at the bottom of Figure 7. Interestingly, the

376 individual photocatalysts in the ternary $BiVO_4$/GQDs/g-C_3N_4 heterostructure shared their

377 electronic cloud density through orbital hybridizations. Whilst, the electronic cloud density map

378 of RGO, g-C_3N_4 and $BiVO_4$ in $BiVO_4$/RGO/g-C_3N_4 heterostructure, show less mutual sharing,

379 especially between RGO and g-C_3N_4. This obvious observation signifies that the GQDs and g-

380 C_3N_4 form a more stable and stronger heterojunction with $BiVO_4$ ($BiVO_4$/GQDs/g-C_3N_4), as

381 evident from its degenerate CDD plot. Moreover, the charge transferring phenomena occurring in

382 this GQDs-ternary heterostructure was higher than the RGO-ternary heterojunction (Figure 7).

383 This statement nicely correlates our experimental data where the GQDs significantly enhanced the

384 photoelectrocatalytic performance than RGO in the ternary heterostructure system.
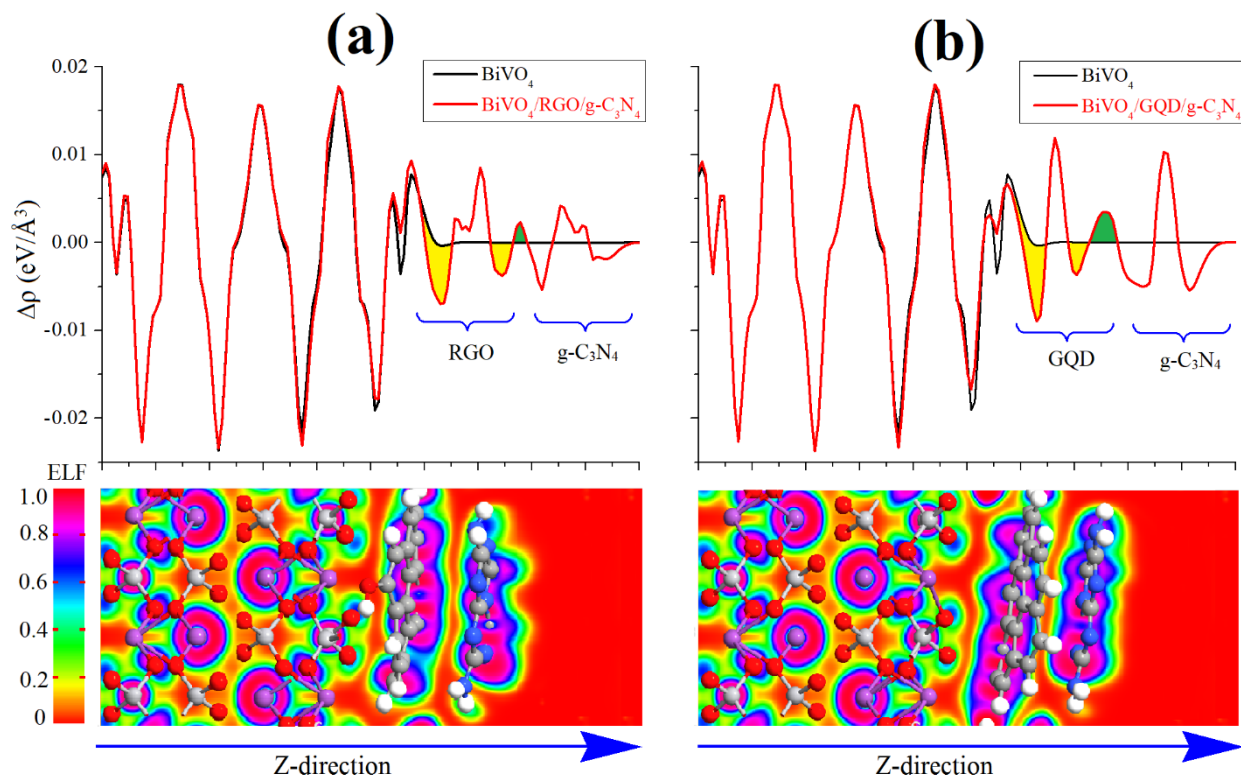
Figure 7: Average electron density difference ($\Delta\rho$) along the Z-direction for (a) $BiVO_4$/RGO/g-C_3N_4 and (b) $BiVO_4$/GQD/g-C_3N_4 along with pristine $BiVO_4$. The green and yellow shaded areas indicate electron accumulation and donation, respectively.

In order to correlate and confirm the high performance of our experimentally observed $BiVO_4$/GQD/g-C_3N_4 photocatalyst, we calculated the band structure and PDOS of the mentioned models. Moreover, the energy bands of a single layer of individual bare samples were also calculated which were depicted in Figure S7 to S12 of the Supporting Information. The simulated bandgaps of $BiVO_4$, $BiVO_4$/g-C_3N_4, $BiVO_4$/RGO/g-C_3N_4 and $BiVO_4$/GQD/g-C_3N_4 were 2.46, 2.46, 2.40, and 2.45 eV, respectively (shown in Figure S7 and Table 2). These simulated bandgaps have a good correlation with our experimentally observed bandgaps of 2.40 eV for $BiVO_4$, 2.80 eV for $BiVO_4$/g-C_3N_4, 2.52 eV for $BiVO_4$/RGO/g-C_3N_4, and 2.47 eV for $BiVO_4$/GQD/g-C_3N_4. It

398 was found that the theoretical data were in accordance with the experimental data which further

399 justified our theoretical protocol as well as validating the significant enhancement of

400 photoelectrocatalytic activity boosted by GQDs.

401 The work function, valence band maximum (VBM), conduction band minimum (CBM),

402 effective masses of electrons and holes of the investigated species were listed in Table 2. $BiVO_4$

403 has an indirect bandgap of 2.46 eV which remains similar upon interaction with $g-C_3N_4$ in the

404 binary heterostructure. However, the direction of the Brillouin zone was changed due to the

405 different geometrical structures of the binary heterostructure. From Figure S11, we can see that

406 upon the interaction of $g-C_3N_4$, RGO, and GQD with $BiVO_4$; extra flat bands were produced in

407 the VB of the ternary heterostructure system. The additional of these flat bands results in the

408 formation of the holes trapping centres which was responsible for minimizing the photocharge

409 carrier recombination. The original VB and CB of $BiVO_4$ in these ternary heterostructures were

410 highlighted with blue and red lines, respectively (Figure S11 and S12). Correspondingly, we can

411 safely infer that the enhanced photocatalytic activity and high photocharge carrier mobility were

412 stemming from these flat bands (*vide supra*). Additionally, the C and N atoms of RGO, GQD, and

413 $g-C_3N_4$, were also contributing to the formation of these additional flat bands (*vide infra*).

414 On the other hand, the effective masses (m_e^* and m_h^*) of the photogenerated charge carriers

415 were measured by fitting the parabolic estimation at both CBM and VBM. The estimation is

416 measured according to Equation 2 where the details of this equation have been discussed

417 previously [23,46].

418 $m^* = \hbar^2 \, (d^2 E/dk^2)^{-1}$ (2)

419   Table 2 summarizes the details of DFT calculations for the effective masses of the

420   photocharge carriers along with the work function (θ), Water molecule adsorption energy (E_{Ad})

421   and other parameters. Theoretically, the lighter the charge carriers' properties along with the larger

422   difference between both effective masses, the more efficient will the photocharge carriers be

423   separated and migrated, thus augmented the overall photoelectrocatalytic performance. According

424   to the DFT calculations tabulated in Table 2, it can be inferred that the effective masses of

425   photogenerated electrons and holes for bare sample, binary and ternary heterostructure systems

426   were substantially lighter, thus responsible for efficient photocatalytic activity. Among all of the

427   studied samples, the $BiVO_4/GQD/g-C_3N_4$ can be considered as the most efficient material owing

428   to its larger difference of 0.45 m_e. This calculation was well aligned with our experimental findings

429   as being discussed above.

430   Table 2: Summarize of all of the DFT analysis which estimated from the calculated band

431   structure along the appropriate Brillouin zone direction.

Species	θ	m_e^*/m_0 (m_e)	m_h^*/m_0 (m_h)	VBM	CBM	ΔE_{gap}	E_{Ad}
$BiVO_4$	5.18	0.02	0.01	-7.03	-4.57	2.46	-2.52
$BiVO_4/g-C_3N_4$	4.43	0.01	0.10	-6.16	-3.70	2.46	-2.84
$BiVO_4/RGO/g-C_3N_4$	4.30	0.67	0.61	-6.57	-4.17	2.40	-3.02
$BiVO_4/GQD/g-C_3N_4$	**4.21**	**0.73**	**0.28**	**-6.41**	**-3.96**	**2.45**	**-3.42**

432

433   It should be noted that the partial density of state (PDOS) is responsible for the contribution

434   of VBM and CBM. The PDOS of the studied binary and ternary heterostructure was examined and

435   the obtained results were illustrated in Figure 8 as well as in Figure S13 and S14 of the Supporting

436   Information. From Figure 8 (a), the VBM and CBM of the $BiVO_4$ were composed of the p orbitals

23

437 originated from the O atoms and 5d orbitals originated from the V atoms, respectively. These VBM

438 and CBM were located at -7.03 and -4.57 eV at vacuum levels. Nevertheless, the VBM of the

439 binary heterostructure system was mainly constituted by the p orbitals of N atoms, responsible for

440 flat bands (*vide supra*). It is noteworthy to mention that the PDOS of N atoms, especially near the

441 VBM was not hybridized with the orbitals of O, C, Bi, and V atoms. In fact, the bands of N at

442 VBM have appeared as separate states which do not increase the overall stability and long-term

443 catalytic activity of binary heterostructure sample. Nonetheless, the CBM of the binary

444 heterostructure system does not change but the density of states of V was reduced compared to

445 that of $BiVO_4$.

446   On the other hand, the PDOS analysis of the ternary heterostructure systems indicates that

447 the orbital hybridization of N atom with O, C, Bi, and V atoms was comparatively stronger than

448 the binary heterostructure photocatalyst as shown in Figure 8 (c and d). Correspondingly, the

449 orbitals of N, Bi, V, C, and O atoms in the VB of the GQD-ternary heterostructure system depicts

450 the strongest hybridization than the other studied photocatalysts. Thus, it can be said that the GQD,

451 $g-C_3N_4$, and $BiVO_4$ in the ternary $BiVO_4/GQD/g-C_3N_4$ system has strong overlapping, responsible

452 for an efficient photoelectrocatalytic hydrogen production. This statement strongly corroborates

453 our experimental observation as well.
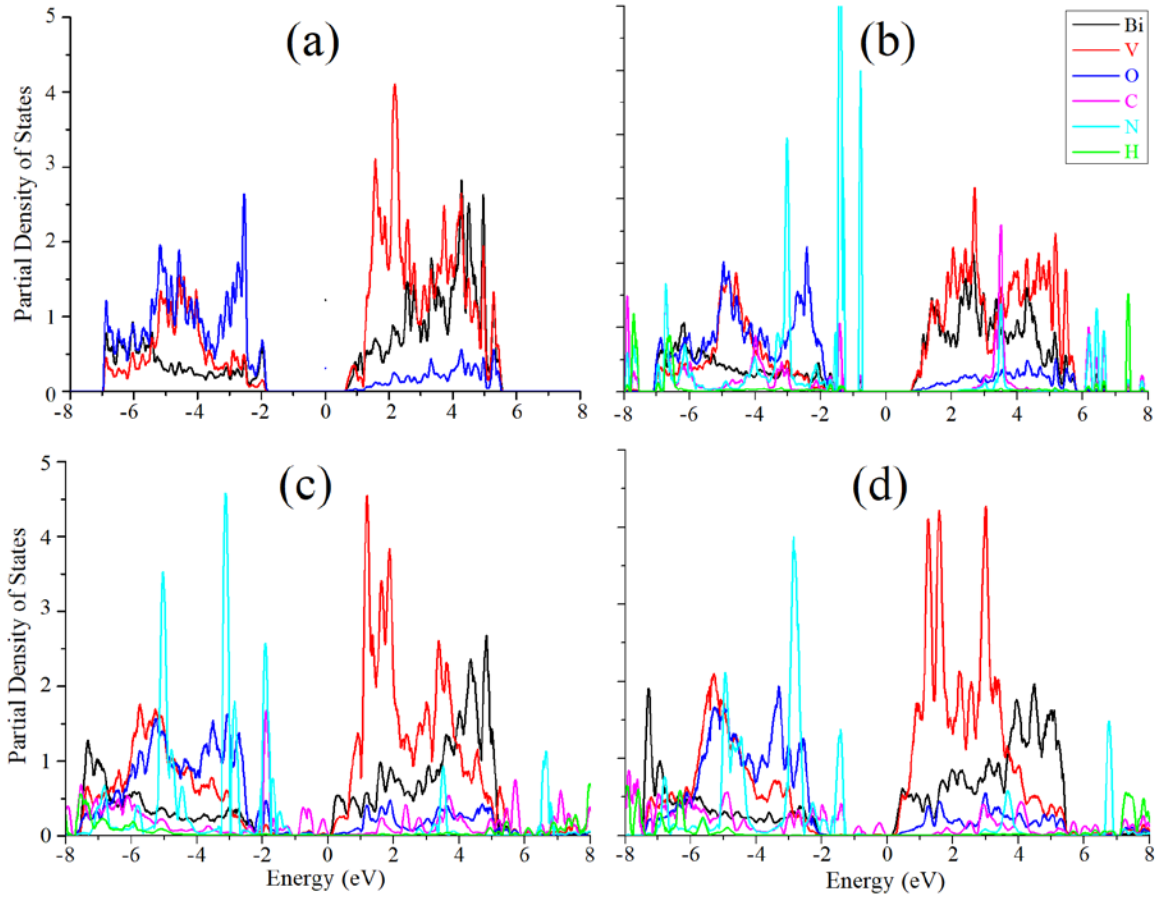
Figure 8: Partial density of states plots of (a) $BiVO_4$, (b) $BiVO_4$/g-C_3N_4, (c) $BiVO_4$/RGO/g-C_3N_4, and (d) $BiVO_4$/GQD/g-C_3N_4 heterojunction; the Fermi energy is set to zero.

The Schematic illustration of the band edge positions for all photocatalysts was shown in Figure 9. The band alignment of the investigated species was calculated according to Equation 3.

$$\Phi = E_{vac} - E_F \tag{3}$$

The simulated work functions of $BiVO_4$, binary heterostructure photocatalyst, RGO-ternary heterostructure photocatalyst and GQDs-ternary heterostructure photocatalyst were 5.18, 4.43, 4.30, and 4.21 eV, respectively (refer Table 2 and Table S1). The simulated work functions suggest

464   that the incorporation of the carbonaceous materials in the ternary heterostructure system improved

465   the photocharge carrier's mobility across the heterostructure interface. Additionally, the obtained

466   work function suggests that the photocharge carrier was moved towards the $BiVO_4$ until the Fermi

467   energy of these units were coordinated.

468   From Figure 9, we can see that the VBM of $BiVO_4$ was higher than the binary and ternary

469   heterostructure photocatalysts. Similarly, the CBM of the $BiVO_4$ was at lower potential (vs.

470   vacuum) than the other studied photocatalysts. Nevertheless, the formation of the heterostructure

471   system has shifted the Fermi energy and the band edge positions to become optimum compared to

472   the individual entities (see Table S1). This shifting position is essential for establishing the internal

473   electric field within the heterostructure system that is responsible for improving the overall

474   photoelectrocatalytic activity. Surprisingly, the change in Fermi energy level (4.21 eV vs. vacuum)

475   and band edge potentials of $BiVO_4$/GQD/g-C_3N_4 were more prominent than the other studied

476   photocatalysts. Thus, this observation further supported that the boosted photoelectrocatalytic

477   performance of the $BiVO_4$/GQD/g-C_3N_4 was mainly due to the ideal position of its VB and CB

478   (straddle with the redox potential of water), and a larger difference between the effective masses

479   of the photocharge carriers (0.45 m_e). As the location of the CB for this ternary heterostructure

480   was higher than the standard H^+/H_2 at the vacuum level, more H^+ were accessible for the reaction

481   to occur, thus a significant amount of H^+ can be converted into H_2. Accordingly, as the CB of this

482   ternary heterostructure photocatalyst was more negative than the standard O_2/H_2O, more water

483   molecules can be oxidized into O_2.
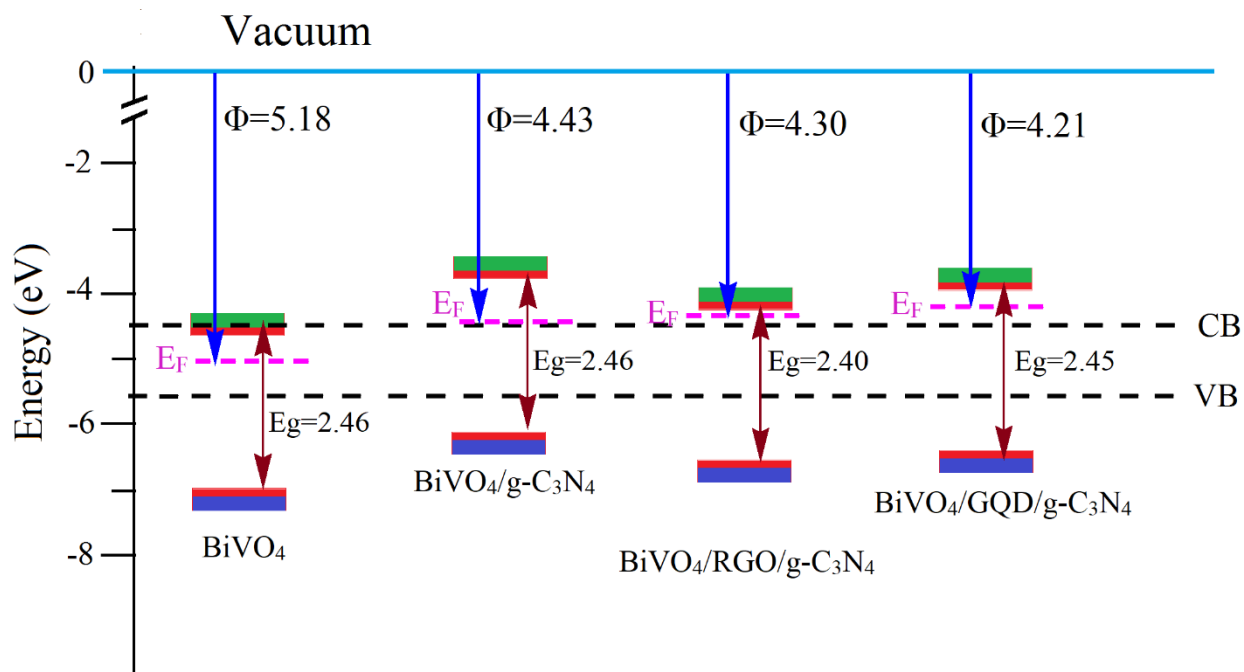
Figure 9: Energy level diagram of the band edge positions of $BiVO_4$, $BiVO_4/g-C_3N_4$, $BiVO_4/RGO/g-C_3N_4$, and $BiVO_4/GQD/g-C_3N_4$.

Finally, we interact water molecules over the surfaces of the studied photocatalysts systems, and allowed to relax, to find the overpotential for water. The optimized relaxed geometries were depicted in Figure 10 and Figure S15, while the per water molecule adsorption energy over the surfaces of investigated species was listed in Table 2. Again, it was found that $BiVO_4/GQD/g-C_3N_4$ has a higher potential for the water molecule, where the per water molecule adsorption energy was -3.42 eV. As shown in Figure 10, some of the water molecules were repelled in the $BiVO_4/RGO/g-C_3N_4$ system which consequently decreased the adsorption energy of water and reduce its catalytic activity. The per water molecule adsorption energy of $BiVO_4@H_2O$, $BiVO_4/g-C_3N_4@H_2O$, and $BiVO_4/RGO/g-C_3N_4@H_2O$ were -2.52, -2.84, and -3.02 eV, respectively.

497
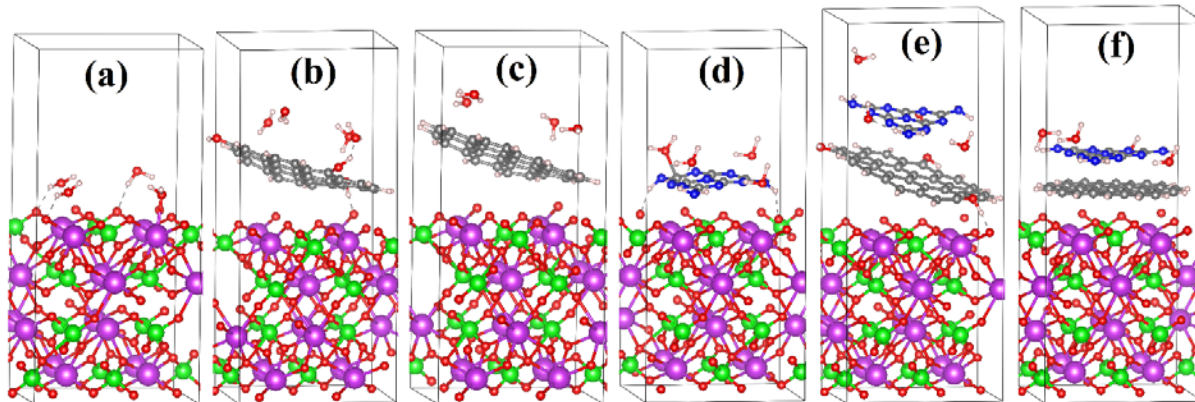
Figure 10: Optimized relaxed structures of (a) $BiVO_4$@H_2O, (b) $BiVO_4$/RGO@H_2O, (c) $BiVO_4$/GQD@H_2O, (d) $BiVO_4$/g-C_3N_4@H_2O, (e) $BiVO_4$/RGO/g-C_3N_4@H_2O, (f) $BiVO_4$/GQD/g-C_3N_4@H_2O.

Conclusion

In summation, the effects of RGO and GQDs as electron mediators on the photoelectrocatalytic hydrogen production of $BiVO_4$/g-C_3N_4 have been studied and further corroborated and counterchecked with DFT analysis. The obtained experimental and computational analyses suggest that the GQDs serves as an excellent electron mediator than RGO within the ternary heterostructure system. Additionally, the ternary $BiVO_4$/GQD/g-C_3N_4 possesses the highest photocurrent density in which ~24% higher than the $BiVO_4$/g-C_3N_4 integrated with RGO. Moreover, the $BiVO_4$/GQD/g-C_3N_4 sample showed the highest photoconversion efficiency in which ~90% enhancement in the efficiency in comparison to the pure sample. Our theoretical simulations strongly support the experimental performance, where it suggests that the atomic orbitals of GQD form strong overlapping with the $BiVO_4$ and g-C_3N_4. Additionally, the ternary $BiVO_4$/GQD/g-C_3N_4 was found to be more stable and have higher interaction energy with a water molecule (-3.42 eV), compared to $BiVO_4$/RGO/g-C_3N_4. Thus, the aforementioned features possess

28

by the ternary $BiVO_4/GQD/g-C_3N_4$ were responsible for boosting the photoelectrocatalytic performance. Thus, for the first time, it was revealed that the addition of GQD in the $BiVO_4/g-C_3N_4$ heterostructure system promotes better photocharge carrier separation and migration than RGO with higher ABPE. This finding offers a new paradigm in the view of the utilization of an electron mediator from the carbonaceous materials in which GQD can be regarded as a more efficient electron mediator than the RGO.

Acknowledgement

References

[1]   J. Jia, W. Sun, Q. Zhang, X. Zhang, X. Hu, E. Liu, J. Fan, Inter-plane heterojunctions within 2D/2D $FeSe_2/g-C_3N_4$ nanosheet semiconductors for photocatalytic hydrogen generation, Appl. Catal. B Environ. 261 (2020) 118249. doi:10.1016/j.apcatb.2019.118249.

[2]   C. Cheng, S. Zong, J. Shi, F. Xue, Y. Zhang, X. Guan, B. Zheng, J. Deng, L. Guo, Facile preparation of nanosized MoP as cocatalyst coupled with $g-C_3N_4$ by surface bonding state for enhanced photocatalytic hydrogen production, Appl. Catal. B Environ. 265 (2020) 118620. doi:10.1016/j.apcatb.2020.118620.

[3]   T. Hisatomi, K. Domen, Reaction systems for solar hydrogen production via water splitting with particulate semiconductor photocatalysts, Nat. Catal. 2 (2019) 387–399. doi:10.1038/s41929-019-0242-6.

537   [4]   H.L. Tan, R. Amal, Y.H. Ng, Alternative strategies in improving the photocatalytic and
538   photoelectrochemical activities of visible light-driven $BiVO_4$: A review, J. Mater. Chem.
539   A. 5 (2017) 16498–16521. doi:10.1039/c7ta04441k.

540   [5]   M.F.R. Samsudin, S. Sufian, B.H. Hameed, Epigrammatic progress and perspective on the
541   photocatalytic properties of $BiVO_4$-based photocatalyst in photocatalytic water treatment
542   technology: A review, J. Mol. Liq. 268 (2018) 438–459. doi:10.1016/j.molliq.2018.07.051.

543   [6]   H. Ullah, A.A. Tahir, S. Bibi, T.K. Mallick, S.Z. Karazhanov, Electronic properties of β-
544   TaON and its surfaces for solar water splitting, Appl. Catal. B Environ. 229 (2018) 24–31.
545   doi:10.1016/j.apcatb.2018.02.001.

546   [7]   M.F.R. Samsudin, H. Ullah, R. Bashiri, N.M. Mohamed, S. Sufian, Y.H. Ng, Experimental
547   and   DFT   Insights   on   Microflower g-C_3N_4/$BiVO_4$ Photocatalyst   for   Enhanced
548   Photoelectrochemical Hydrogen Generation from Lake water, ACS Sustain. Chem. Eng. 8
549   (2020) 9393−9403. doi:10.1021/acssuschemeng.0c02063.

550   [8]   M.F.R. Samsudin, S. Sufian, Hybrid 2D/3D g-C_3N_4/$BiVO_4$ photocatalyst decorated with
551   RGO for boosted photoelectrocatalytic hydrogen production from natural lake water and
552   photocatalytic   degradation   of   antibiotics,   J.   Mol.   Liq.   314   (2020)   113530.
553   doi:10.1016/j.molliq.2020.113530.

554   [9]   H. Wu, H.L. Tan, C.Y. Toe, J. Scott, L. Wang, R. Amal, Y.H. Ng, Photocatalytic and
555   Photoelectrochemical Systems: Similarities and Differences, Adv. Mater. 32 (2020)
556   1904717. doi:10.1002/adma.201904717.

557   [10]   M.F.R. Samsudin, C. Frebillot, Y. Kaddoury, S. Sufian, W.J. Ong, Bifunctional Z-Scheme
558   Ag/$AgVO_3$/g-C_3N_4 photocatalysts for expired ciprofloxacin degradation and hydrogen
559   production from natural rainwater without using scavengers, J. Environ. Manage. 270
560   (2020) 110803. doi:10.1016/j.jenvman.2020.110803.

561   [11]   Y. Ren, D. Zeng, W. Ong, Interfacial engineering of graphitic carbon nitride (g-C_3N_4) -
562   based metal sulfide heterojunction photocatalysts for energy conversion : A review, Chinese
563   J. Catal. 40 (2019) 289–319. doi:10.1016/S1872-2067(19)63293-6.

564 [12] J. Wang, C. Liu, S. Yang, X. Lin, W. Shi, Fabrication of a ternary heterostructure $BiVO_4$

565 quantum dots/C60/g-C_3N_4 photocatalyst with enhanced photocatalytic activity, J. Phys.

566 Chem. Solids. 136 (2020) 109164. doi:10.1016/j.jpcs.2019.109164.

567 [13] R.A. Rather, I.M.C. Lo, Photoelectrochemical sewage treatment by a multifunctional g-

568 C_3N_4/Ag/AgCl/$BiVO_4$ photoanode for the simultaneous degradation of emerging pollutants

569 and hydrogen production, and the disinfection of E. coli, Water Res. 168 (2020) 115166.

570 doi:10.1016/j.watres.2019.115166.

571 [14] W.J. Ong, L.L. Tan, Y.H. Ng, S.T. Yong, S.P. Chai, Graphitic Carbon Nitride (g-C_3N_4)-

572 Based Photocatalysts for Artificial Photosynthesis and Environmental Remediation: Are

573 We a Step Closer to Achieving Sustainability?, Chem. Rev. 116 (2016) 7159–7329.

574 doi:10.1021/acs.chemrev.6b00075.

575 [15] Y. Wang, J. Sun, J. Li, X. Zhao, Electrospinning Preparation of Nanostructured g-C_3N_4

576 /$BiVO_4$ Composite Films with an Enhanced Photoelectrochemical Performance, Langmuir.

577 33 (2017) 4694–4701. doi:10.1021/acs.langmuir.7b00893.

578 [16] J. Safaei, H. Ullah, N.A. Mohamed, M.F. Mohamad Noh, M.F. Soh, A.A. Tahir, N. Ahmad

579 Ludin, M.A. Ibrahim, W.N.R. Wan Isahak, M.A. Mat Teridi, Enhanced

580 photoelectrochemical performance of Z-scheme g-C_3N_4 /$BiVO_4$ photocatalyst, Appl. Catal.

581 B Environ. 234 (2018) 296–310. doi:10.1016/j.apcatb.2018.04.056.

582 [17] M.F.R. Samsudin, A. Mahmood, S. Sufian, Enhanced photocatalytic degradation of

583 wastewater over RGO-TiO_2/$BiVO_4$photocatalyst under solar light irradiation, J. Mol. Liq.

584 268 (2018) 26–36. doi:10.1016/j.molliq.2018.05.012.

585 [18] Q. Wang, D. Astruc, State of the Art and Prospects in Metal-Organic Framework (MOF)-

586 Based and MOF-Derived Nanocatalysis, Chem. Rev. 120 (2020) 1438–1511.

587 doi:10.1021/acs.chemrev.9b00223.

588 [19] F. He, Z. Wang, Y. Li, S. Peng, B. Liu, The nonmetal modulation of composition and

589 morphology of g-C_3N_4-based photocatalysts, Appl. Catal. B Environ. 269 (2020) 118828.

590 doi:10.1016/j.apcatb.2020.118828.

[20] B.D. Pan, J. Zhang, Z. Li, M. Wu, Hydrothermal Route for Cutting Graphene Sheets into Blue-Luminescent Graphene Quantum Dots, Adv. Mater. 22 (2010) 734–738. doi:10.1002/adma.200902825.

[21] M.F.R. Samsudin, R. Bashiri, N.M. Mohamed, Y.H. Ng, S. Sufian, Tailoring the morphological structure of $BiVO_4$ photocatalyst for enhanced photoelectrochemical solar hydrogen production from natural lake water, Appl. Surf. Sci. 504 (2020) 144417. doi:10.1016/j.apsusc.2019.144417.

[22] H. Ullah, A.A. Tahir, T.K. Mallick, Structural and electronic properties of oxygen defective and Se-doped p-type $BiVO_4(001)$ thin film for the applications of photocatalysis, Appl. Catal. B Environ. 224 (2018) 895–903. doi:10.1016/j.apcatb.2017.11.034.

[23] M. Sookhakian, H. Ullah, M.A. Mat Teridi, G.B. Tong, W.J. Basirun, Y. Alias, Boron-doped graphene-supported manganese oxide nanotubes as an efficient non-metal catalyst for the oxygen reduction reaction, Sustain. Energy Fuels. 4 (2020) 737–749. doi:10.1039/c9se00775j.

[24] G. Kresse, D. Joubert, From ultrasoft pseudopotentials to the projector augmented-wave method, Phys. Rev. B. 59 (1999) 1758–1775. doi:10.1103/PhysRevB.59.1758.

[25] F. Tran, P. Blaha, Accurate band gaps of semiconductors and insulators with a semilocal exchange-correlation potential, Phys. Rev. Lett. 102 (2009) 5–8. doi:10.1103/PhysRevLett.102.226401.

[26] J. Endres, D.A. Egger, M. Kulbak, R.A. Kerner, L. Zhao, S.H. Silver, G. Hodes, B.P. Rand, D. Cahen, L. Kronik, A. Kahn, Valence and Conduction Band Densities of States of Metal Halide Perovskites: A Combined Experimental-Theoretical Study, J. Phys. Chem. Lett. 7 (2016) 2722–2729. doi:10.1021/acs.jpclett.6b00946.

[27] M.F.R. Samsudin, N. Bacho, S. Sufian, Y.H. Ng, Photocatalytic degradation of phenol wastewater over Z-scheme g-C_3N_4/CNT/$BiVO_4$ heterostructure photocatalyst under solar light irradiation, J. Mol. Liq. 277 (2019) 977–988. doi:10.1016/j.molliq.2018.10.160.

[28]　M.F.R. Samsudin, S. Sufian, R. Bashiri, N.M. Mohamed, R.M. Ramli, Synergistic effects of pH and calcination temperature on enhancing photodegradation performance of m-$BiVO_4$, J. Taiwan Inst. Chem. Eng. 81 (2017) 305–315. doi:10.1016/j.jtice.2017.09.045.

[29]　M.K.A. Ahmad Madzlan, M.F.R. Samsudin, F. Maeght, C. Goepp, S. Sufian, Enhancement of g-C_3N_4 via Acid Treatment for the Degradation of Ciprofloxacin Antibiotic, Malaysian J. Microsc. 16 (2020) 105–114.

[30]　Y. Wang, G. Tan, T. Liu, Y. Su, H. Ren, X.L. Zhang, A. Xia, L. Lv, Y. Liu, Photocatalytic properties of the g-C_3N_4/{010} facets $BiVO_4$ interface Z-Scheme photocatalysts induced by $BiVO_4$ surface heterojunction, Appl. Catal. B Environ. 234 (2018) 37–49. doi:10.1016/j.apcatb.2018.04.026.

[31]　M.F.R. Samsudin, A. Dumas, R. Bashiri, N.M. Muti, S. Sufian, Development of the g-C_3N_4 /$BiVO_4$ Microflower Photocatalyst for Photocatalytic Degradation of Amoxicillin and Hydrogen Production, Malaysian J. Microsc. 16 (2020) 180–187.

[32]　Y.-Z. Liu, C.-M. Chen, Y.-F. Li, X.-M. Li, Q.-Q. Kong, M.-Z. Wang, Crumpled reduced graphene oxide by flame-induced reduction of graphite oxide for supercapacitive energy storage, J. Mater. Chem. A. 2 (2014) 5730–5737.

[33]　A. Yuan, H. Lei, F. Xi, J. Liu, L. Qin, Z. Chen, X. Dong, Graphene quantum dots decorated graphitic carbon nitride nanorods for photocatalytic removal of antibiotics, J. Colloid Interface Sci. 548 (2019) 56–65. doi:10.1016/j.jcis.2019.04.027.

[34]　X. Yu, Z. Zhao, N. Ren, J. Liu, D. Sun, L. Ding, H. Liu, Top or Bottom, Assembling Modules Determine the Photocatalytic Property of the Sheetlike Nanostructured Hybrid Photocatalyst Composed with Sn_3O_4 and rGO (GQD), ACS Sustain. Chem. Eng. 6 (2018) 11775–11782. doi:10.1021/acssuschemeng.8b02030.

[35]　C. Wang, Y. Zhao, H. Xu, Y. Li, Y. Wei, J. Liu, Z. Zhao, Efficient Z-scheme photocatalysts of ultrathin g-C3N4-wrapped Au/TiO_2-nanocrystals for enhanced visible-light-driven conversion of CO_2 with H_2O, Appl. Catal. B Environ. 263 (2020) 118314. doi:10.1016/j.apcatb.2019.118314.

644 [36] S. Wang, Y. Liu, J. Wang, Iron and sulfur co-doped graphite carbon nitride (FeOy/S-g-
645   C_3N_4) for activating peroxymonosulfate to enhance sulfamethoxazole degradation, Chem.
646   Eng. J. 382 (2020) 122836. doi:10.1016/j.cej.2019.122836.

647 [37] G. Singh, R. Vaish, Melt quenched V_2O_5/BiVO$_4$ composite: A novel and promising
648   adsorbent   and   photocatalyst,   Mater.   Chem.   Phys.   240   (2020)   122238.
649   doi:10.1016/j.matchemphys.2019.122238.

650 [38] B. Zhang, L. Chou, Y. Bi, Tuning surface electronegativity of BiVO$_4$ photoanodes toward
651   high-performance   water   splitting,   Appl.   Catal.   B   Environ.   262   (2020)   118267.
652   doi:10.1016/j.apcatb.2019.118267.

653 [39] W. Ong, L. Tan, S. Chai, S. Yong, A. Rahman, Surface charge modification via protonation
654   of graphitic carbon nitride (g-C_3N_4) for electrostatic self-assembly construction of 2D/2D
655   reduced graphene oxide (rGO)/g-C_3N_4 nanostructures toward enhanced photocatalytic
656   reduction of carbon dioxide to methane, Nano Energy. 13 (2015) 757–770.
657   doi:10.1016/j.nanoen.2015.03.014.

658 [40] Y. Zhang, G. Wang, Z. Jin, An orderly assembled g-C_3N_4, rGO and Ni 2 P photocatalyst
659   for efficient hydrogen evolution, Int. J. Hydrogen Energy. 44 (2019) 10316–10327.
660   doi:10.1016/j.ijhydene.2019.03.006.

661 [41] M. Li, G. Xu, Z. Guan, Y. Wang, H. Yu, Y. Yu, Synthesis of Ag/BiVO$_4$/rGO composite
662   with enhanced photocatalytic degradation of triclosan, Sci. Total Environ. 664 (2019) 230–
663   239. doi:10.1016/j.scitotenv.2019.02.027.

664 [42] Y. Dong, S. Zhang, L. Shi, Y. Chen, J. Ma, S. Guo, X. Chen, H. Song, The
665   photoluminescence of step-wise reduced graphene oxide quantum dots, Mater. Chem. Phys.
666   203 (2018) 125–132. doi:10.1016/j.matchemphys.2017.09.064.

667 [43] H. Zhang, Y. Cao, L. Zhong, X. Cao, J. He, J. Sun, W. Lei, Fast photogenerated electron
668   transfer in N-GQDs / PTI / ZnO-QDs ternary heterostructured nanosheets for photocatalytic
669   H 2 evolution under visible light, Appl. Surf. Sci. 485 (2019) 361–367.
670   doi:10.1016/j.apsusc.2019.04.230.

671 [44] M.F.R. Samsudin, P.J. Jayabalan, W.J. Ong, Y.H. Ng, S. Sufian, Photocatalytic degradation
672   of real industrial poultry wastewater via platinum decorated $BiVO_4$ / $g\text{-}C_3N_4$ photocatalyst
673   under solar light irradiation, J. Photochem. Photobiol. A Chem. 378 (2019) 46–56.
674   doi:10.1016/j.jphotochem.2019.04.013.

675 [45] X. Cao, C. Xu, X. Liang, J. Ma, M. Yue, Y. Ding, Rationally designed/assembled hybrid
676        $BiVO_4$-based photoanode for enhanced photoelectrochemical performance, Appl. Catal. B
677   Environ. 260 (2020) 118136. doi:10.1016/j.apcatb.2019.118136.

678 [46] S.N.F.M. Nasir, H. Ullah, M. Ebadi, A.A. Tahir, J.S. Sagu, M.A.M. Teridi, New insights
679   into $Se/BiVO_4$ heterostructure for photoelectrochemical water splitting: A combined
680   experimental and DFT study, J. Phys. Chem. C. 121 (2017) 6218–6228.
681   doi:10.1021/acs.jpcc.7b01149.

682 [47] J. Liu, Origin of High Photocatalytic Efficiency in Monolayer $g\text{-}C_3N_4$/CdS Heterostructure:
683   A Hybrid DFT Study, J. Phys. Chem. C. 119 (2015) 28417–28423.
684   doi:10.1021/acs.jpcc.5b09092.

685 [48] M. Niu, D. Cheng, D. Cao, Understanding the mechanism of photocatalysis enhancements
686   in the graphene-like semiconductor sheet/TiO_2 composites, J. Phys. Chem. C. 118 (2014)
687   5954–5960. doi:10.1021/jp412556r.

688